Optimal structure design of a sugarcane harvester extractor based on CFD

Baocheng Zhou[1], Jichen Han[1], Zhijie Wu[1], Fei Feng[1*], Shaochun Ma[1,2*]

(1. *College of Engineering, China Agricultural University, Beijing 100083, China*;
2. *State Key Laboratory of Intelligent Agricultural Power Equipment, Luoyang 471039, Henan, China*)

Abstract: To address the challenges of high impurity rate and cane loss rate in mechanized sugarcane harvesting, the internal flow field of the extractor was analyzed through computational fluid dynamics (CFD) simulation, and the structure of the extractor was optimized to improve the harvesting quality. The simulation model was validated by comparing simulated and experimental wind speeds at the extractor outlet, yielding a maximum error of 5.29% and an average error of 4.71%, confirming the model's accuracy. The analysis revealed that abrupt changes in structural geometry lead to significant airflow vortices within the discharge hood, a backflow phenomenon at the outlet, and additional vortices in the cleaning chamber, all of which ultimately result in high impurity rate and cane loss rate. To address these issues, the extractor's structure was optimized, the outer contour of the discharge hood was designed as a smooth arc curve, and the lower air inlet of the cleaning chamber was changed from rectangular to circular, which eliminated the vortices and improved airflow uniformity. The impurity rate test showed that when the harvester driving speed was 1 km/h, the impurity rate level before and after optimization was comparable across different rotational speeds. At 2 km/h, the low-speed performance (1250 r/min) was significantly improved, reducing the impurity rate by 21.52%. At 3 km/h, the impurity rate decreased by 19.84% and 28.30% at low and medium speeds (1450 r/min), respectively. The cane loss rate test demonstrated that when the extractor speed was 1250 r/min, the difference before and after optimization was minimal. At 1450 r/min, the cane loss rate decreased significantly, with a maximum decrease of 10.75%. At 1650 r/min, the cane loss rate decreased by 8.78% at most. The optimized extractor significantly reduced the impurity rate and cane loss rate at higher harvester speeds (2-3 km/h), making it suitable for large-scale and high-speed harvesting operations and improving the harvesting efficiency. The research results will help to design and improve the performance of the extractor, thus improving the harvest quality and increasing farmers' income.

Keywords: sugarcane harvest, CFD, extractor, structural optimization
DOI: 10.25165/j.ijabe.20251804.9323

Citation: Zhou B C, Han J C, Wu Z J, Feng F, Ma S C. Optimal structure design of a sugarcane harvester extractor based on CFD. Int J Agric & Biol Eng, 2025; 18(4): 117–127.

1 Introduction

Sugarcane is an important cash crop and a source of sugar, grown mainly in regions such as Brazil, India, and China. Currently, China ranks as the third largest producer of sugarcane in the world, with its production accounting for about 90% of the total domestic sugar output. However, domestic sugar production meets only about 70% of demand, with the remaining 30% relying on imports[1-3]. The primary reason for the downturn in China's sugarcane industry is the low level of mechanization—particularly in mechanized harvesting. A key factor contributing to this issue is the high impurity rate and cane loss associated with mechanized harvesting[4-6]. As a crucial component of the sugarcane chopper harvester, the impurity removal extractor plays a decisive role in the overall operational performance, especially in terms of impurity removal. Currently, mechanically harvested sugarcane has an impurity rate of around 10% and a cane loss rate of approximately 10%. However, due to limitations in our country's current sugar-making equipment and processes, sugar factories require the impurity rate of sugarcane to be below 5%[7,8]. The impurity rate and loss rate are high, which causes farmers' economic losses. At the same time, due to the limitations of sugar-making equipment and technology in China, sugar factories require the impurity rate of sugarcane to be below 5%. All these greatly limit the development and popularization of mechanized harvesting. Therefore, it is imperative to improve the performance of the impurity removal extractor to reduce both impurity rate and cane loss.

In the research on the impurity removal extractor of sugarcane harvester, Whiteing et al.[9] conducted an experimental study on the selection of extractor speed and sugarcane feeding volume, and found that increasing the feeding volume seriously affects the impurity removal effect of the extractor, and that increasing the extractor speed will significantly increase the loss rate. Sichter et al.[10] proposed using sugar loss as an evaluation metric to overcome the inaccuracies of existing methods, thereby identifying optimal operating parameters for the extractor. Similarly, Viator et al.[11] investigated the effects of forward speed and extractor speed on decontamination efficiency. Wang et al.[12] demonstrated that a higher wind speed could effectively reduce impurity rate by exploiting differences in suspension speeds between cane segments and impurities. Although these studies provide valuable guidance on operational parameter settings, they largely overlook the underlying structural and aerodynamic factors that govern performance. To bridge this gap, researchers have employed computational fluid dynamics (CFD) to analyze the internal flow fields of impurity

Received date: 2024-08-27 **Accepted date:** 2025-04-11
Biographies: Baocheng Zhou, PhD candidate, research interest: agricultural machinery and equipment design, Email: 157243425@qq.com; **Jichen Han**, MS candidate, research interest: agricultural machinery and equipment design, Email: s20233071467@cau.edu.cn; **Zhijie Wu**, MS candidate, research interest: agricultural machinery and equipment design, Email: 2904321677@qq.com
***Corresponding author: Fei Feng**, PhD, Associate Professor, research interest: agricultural machinery and equipment design, Tel: +86-15927535128, Email: fengfeigood@163.com; **Shaochun Ma**, PhD, Professor, research interest: sugarcane intelligent harvesting equipment. College of Engineering, China Agricultural University, Beijing 100083, China. Tel: +86-18800123546, Email: shaochun2004@cau.edu.cn.

removal devices. Huang et al.[13] used Fluent software to analyze the flow field of the trash removal fan. The results indicated that the static pressure, dynamic pressure, and total pressure at the upstream of the impeller were distinct and the gradient was small. Nong et al.[14] utilized flow simulation to examine how impeller speed and the position of key components influence performance. Zhou et al.[15] introduced a method that combines blade element theory with CFD to analyze the energy consumption and internal flow characteristics of the extractor. By focusing on the mechanisms behind the extractor's performance, they were able to optimize the structural parameters, leading to potential energy savings and enhanced operational efficiency. Despite these advances, comprehensive solutions to address poor aerodynamic performance and suboptimal impurity removal have not yet been achieved.

In response, some scholars have shifted focus toward structural optimization. Xie et al.[16] designed an impurity removal extractor by determining optimal parameters—such as rotational speed, air inlet method, and air inlet area—based on outlet wind speed measurements, though without assessing the actual impurity removal effect. Wang et al.[17] used the isolated blade type method to design the extractor and verified the aerodynamic performance of the extractor by CFD simulation, but their study was limited only to the extractor blades. Xing et al.[18-20] optimized extractor cowls and blades to improve aerodynamic performance and reduce both impurity rate and cane loss, albeit without addressing the negative pressure structure. Ren et al.[21] further optimized the negative pressure structure of the extractor, contributing valuable insights into reducing impurity rate and cane loss.

In summary, previous research on extractor performance has predominantly focused on parameter optimization and simulation analysis, with relatively little attention given to the design and optimization of the overall structure of the extractor. Consequently, the performance improvements achieved have been limited and do not fully meet harvesting requirements. In contrast, studies on pneumatic cleaning devices for grain harvesters are more advanced. Wang et al.[22] designed a helical variable-angle impeller for a cross-flow extractor and optimized the volute geometry; experimental results confirmed that the extractor met the flow field distribution requirements for both pre-cleaning and wind screening. Similarly, Gebrehiwot et al.[23] enhanced a centrifugal extractor by incorporating cross-flow openings, which significantly increased flow rate under low-load conditions and addressed issues of insufficient wind force caused by narrow outlet areas and screen blockages. Furthermore, Tong et al.[24] performed CFD simulations on the flow fields of extractors and cleaning drums, proposing structural improvements that enhanced airflow uniformity; their optimized design resulted in a loss rate of 0.91% and an impurity rate of 0.87% during rice harvesting, and a loss rate of 0.82% with an impurity rate of 0.76% during wheat harvesting. These studies demonstrate that structural modifications can markedly improve extractor performance.

Therefore, to address the high impurity rate and cane loss observed in sugarcane harvesters after impurity removal, this study employed numerical simulation to analyze the aerodynamic deficiencies of the sugarcane harvester extractor. An overall structural improvement scheme for the cleaning device is proposed and validated through prototype experiments. The performance of the extractor before and after optimization is evaluated based on impurity rate and cane loss, thereby providing guidance for the overall design of impurity removal extractors in sugarcane harvesters and contributing to reduced impurity rate and cane loss.

2 Current extractor structure and aerodynamic performance analysis

2.1 Structure and working principle of the current extractor

The 4GQ-180 sugarcane harvester's extractor, developed by Luoyang Chenhan Agricultural Equipment Technology Co., Ltd., was composed of a cleaning chamber, deflector plate, extractor blades, discharge hood, and drive shaft as shown in Figure 1, and the main parameters are listed in Table 1. During the impurity removal process, cane sections and impurities were simultaneously introduced into the extractor. Impurities with lower suspension speeds, such as cane leaves, were discharged through the outlet of the discharge hood under the influence of negative pressure. Meanwhile, cane sections, which had higher suspension speeds, fell directly into the collecting device beneath the extractor due to the force of gravity (aligned with the negative direction of the *Z*-axis).

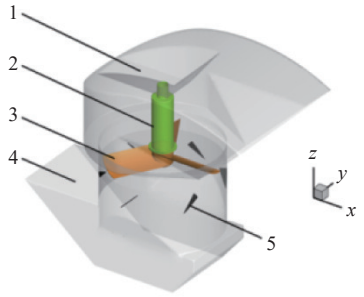

1. Discharge hood 2. Drive shaft 3. Extractor blades 4. Cleaning chamber 5. Deflector plate

Figure 1 Structure of the current impurity removal extractor

Table 1 Main parameters of the current de-hybridizing extractor

Parameters	Values
Diameter of impeller/mm	850
Number of blades	3
Diameter of extractor/mm	900
Number of deflectors	6
Rotation speed /r·min^{-1}	1250-1650

2.2 Airflow modeling and meshing

The flow field of the extractor was modeled in SolidWorks 2022 (Figure 2). To simulate the external environment as realistically as possible, cylindrical and rectangular extensions, with dimensions larger than the diameter of the extractor, were added at the inlet and outlet locations of the extractor, respectively, thereby reducing boundary effects, promoting fully developed flow, and enhancing simulation accuracy. The model was saved in X-T format and imported into Fluent Meshing for meshing (Figure 3). The face mesh of the model was filled with a polyhedral mesh, and the volume mesh was filled with Poly-Hexcore mesh. The Poly-

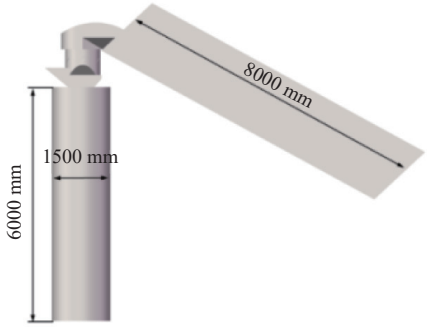

Figure 2 Calculation domain of flow field

Hexcore meshing method effectively reduced the number of meshes and accelerated the calculation speed. Compared to the tetrahedral mesh, the Poly-Hexcore mesh exhibited higher mesh quality, as well as improved convergence speed and accuracy in the calculations.

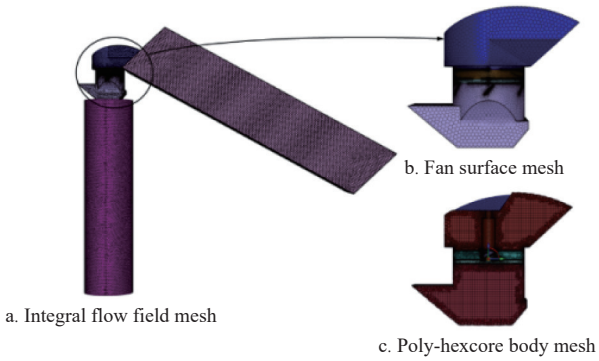

Figure 3 Mesh model of the extractor

2.3 Control equations and boundary conditions

2.3.1 Turbulence model

To make the fluid simulation closer to the actual situation, the best method for calculating the turbulent flow should be determined first before the calculation. Currently there are three main numerical simulation methods for turbulence: Direct Numerical Simulation (DNS), Large Eddy Simulation (LES), and Reynolds-Averaged Navier-Stokes (RANS) equations[25-27]. The Reynolds-Averaged Navier-Stokes (RANS) model is the most widely used method in engineering calculations[28,29]. The turbulence model used in this paper is the Realizable k-ε model. The governing equations for the Realizable k-ε turbulence model are as follows:

$$\frac{\partial \bar{u}_i}{\partial x_i} = 0 \tag{1}$$

$$\rho \bar{u}_j \frac{\partial \bar{u}_i}{\partial x_i} = \frac{\partial \bar{p}}{\partial x_i} + \mu \frac{\partial^2 \bar{u}_i}{\partial x_j \partial x_j} + \frac{\partial}{\partial x_j}\left(-\rho \bar{\acute{u}}_i \bar{\acute{u}}_j\right) \tag{2}$$

$$\rho \frac{\partial (k\bar{u}_i)}{\partial x_i} = \frac{\partial}{\partial x_i}\left[\left(\mu + \frac{\mu_t}{\sigma_k}\right)\frac{\partial k}{\partial x_j}\right] + G_k - \rho\varepsilon \tag{3}$$

$$\rho \frac{\partial (\varepsilon\bar{u}_i)}{\partial x_i} = \frac{\partial}{\partial x_j}\left[\left(\mu + \frac{\mu_t}{\sigma_\varepsilon}\right)\frac{\partial \varepsilon}{\partial x_j}\right] + \rho C_1 E_\varepsilon - \rho C_2 \frac{\varepsilon^2}{k + \sqrt{\nu\varepsilon}} \tag{4}$$

where, $\bar{u}_i$ is the time-averaged velocity component in the i-direction, m/s; $\acute{u}$ is the fluctuating velocity component in the i-direction, m/s; $\bar{p}$ is the time-averaged pressure, Pa; x_i is the spatial coordinate in the i-direction; ρ is the fluid density, kg/m^3; μ is the dynamic viscosity, Pa·s; k is the turbulent kinetic energy, J; ε is the turbulent dissipation rate; $\sigma_k = 1.0; \sigma_\varepsilon = 1.2$; G_k is the turbulent kinetic energy generated by the mean velocity gradient; $C_1 = \max\left(0.43, \frac{\psi}{\psi+5}\right)$; $\psi = \frac{Ek}{\varepsilon}$, where E is the average rate of strain tensor, $E = \sqrt{2E_{ij}E_{ij}}$; $C_2 = 1.9$.

2.3.2 Rotating model and boundary conditions

The computational model of the extractor comprised a rotating dynamic region and a stationary static region, with the extractor blade area designated as the dynamic region while the remaining areas were treated as static. The interface between the rotating and non-rotating regions was addressed using both the Multiple Reference Frame (MRF) method and the Mesh Motion method. The MRF method simplified the internal flow field of the extractor to the instantaneous flow field at a specific blade position, thereby solving the unsteady problem with a steady-state approach. Compared with the Mesh Motion method, it significantly reduced the computational load and was better suited for models with high computational demands. Therefore, the MRF method was adopted. The model's inlet and outlet were configured as a pressure inlet and a pressure outlet, respectively, with the pressure set to atmospheric conditions for simulating the no-load extractor flow field. The wall boundary was defined as a no-slip condition, and the internal interfaces were set as interfaces to ensure proper data transfer across contact surfaces. A first-order upwind discretization scheme was employed, and the SIMPLE algorithm was used for solution. The turbulence model was Realizable k-ε model. The turbulence intensity was set to 5% and the turbulence viscosity ratio to 10. The steady-state solution model was selected, and the number of simulation iterations was 3000.

2.4 Verification of mesh independence

Performing mesh independence verification is crucial to ensure the reliability and accuracy of simulation results. It helps identify the optimal mesh size, balancing computational efficiency and precision. Mesh independence verification was performed at a rotational speed of 1650 r/min. The same meshing method was applied, and the surface of the impurity removal extractor was refined to varying degrees, resulting in different mesh quantities. Five types of meshes were selected for verification. In Fluent, the impeller torque and no-load wind speed of the flow field were measured and used as evaluation criteria.

The results, shown in Figure 4, indicated that the initial mesh contained approximately 9.0×10^5 elements. As the number of elements increased to around 3.3×10^6, the computational model's indicators tended to stabilize. Following a comprehensive evaluation of accuracy and computational time, a mesh comprising 3.3×10^6 elements was adopted for the calculations.

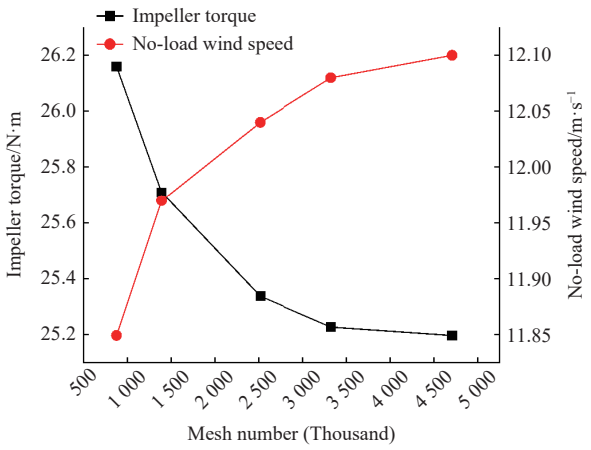

Figure 4 Mesh independence verification of the current extractor

2.5 Verification of simulation results

To verify the accuracy of the computational results, the average wind speed at the extractor outlet was calculated and measured at extractor speeds ranging from 1250 to 1650 r/min. The accuracy was assessed by comparing the calculated results with the measured values and evaluating the error between them.

2.5.1 Measurement device and method

The wind speed at the outlet of the prototype extractor at different rotational speeds was measured using an anemometer from Dongguan Xintai Instrument Co., Ltd. (Model: HT-9829; Resolution: 0.01 m/s) to validate the simulation results. As shown in Figure 5, the extractor outlet was divided into nine regions. The wind speed was first measured in each region separately. Then, the wind speed in each region was multiplied by the corresponding area to calculate the flow rate for that region. Finally, the flow rates of

all regions were summed and divided by the total area of the extractor outlet to obtain the average wind speed at the outlet. The calculation formula is as follows:

$$v_o = \frac{\sum_{i=1}^{9} v_i \cdot S_i}{S_o} \quad (5)$$

where, v_o is the average wind speed at the outlet, m/s; v_i is the measured wind speed in the corresponding region, m/s; S_i is the area of the corresponding region, m^2; S_o is the area of the extractor outlet, m^2.

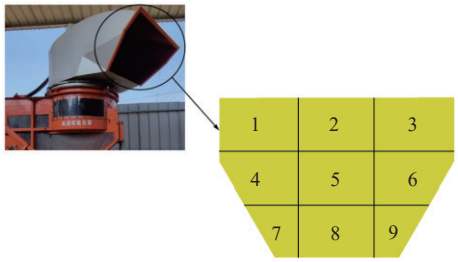

Figure 5 Schematic diagram of wind speed measurement area division

2.5.2 Measurement results

Table 2 presents the simulated and measured values of extractor outlet wind speed at different rotational speeds. The maximum error in the calculated average wind speed at the extractor outlet for each rotational speed was 5.29%, and the average error was 4.71%. Since the errors were within 10%, the numerical simulation was deemed to be highly accurate.

Table 2 Simulated and measured values of outlet wind speed at different rotational speeds

Extractor speed/r·min^{-1}	No-load wind speed v/m·s^{-1}		Error/%
	Simulation value	Measured value	
1250	9.01	9.40	4.32
1450	10.37	10.84	4.53
1650	12.08	12.72	5.29

3 Analysis of current extractor internal flow simulation results

Figure 6 presents the streamline distribution of the internal flow field at different speeds. When analyzing the airflow distribution inside the extractor, it was found that different speeds did not significantly change the distribution patterns; only the numerical values at various positions varied, as shown in Figure 6. As the extractor speed increased, the velocity of internal streamlines also increased, while the overall distribution pattern remained largely unchanged. All three speeds exhibited large low-speed vortices behind the discharge hood and concentrated streamlines above the outlet. Considering energy consumption and efficiency during actual operation, the extractor was typically operated at a medium speed of 1450 r/min; therefore, only the simulation results at 1450 r/min were analyzed in detail.

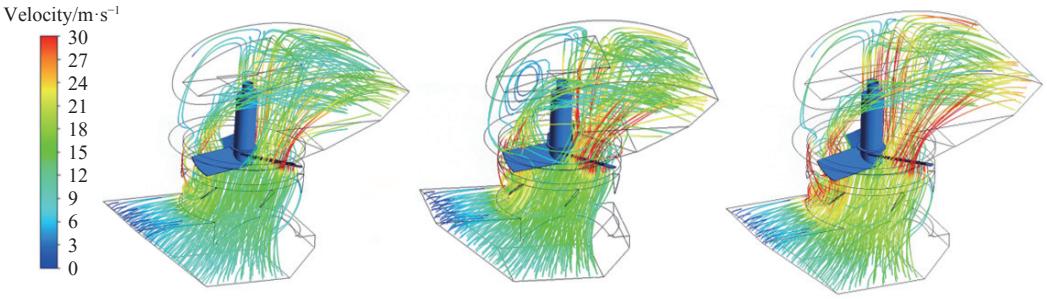

a. 1250 r/min b. 1450 r/min c. 1650 r/min

Figure 6 Streamline distribution of the internal flow field at different speeds

3.1 Analysis of the internal flow field in the current extractor discharge hood

3.1.1 Analysis of wind pressure in the current extractor discharge hood

Figure 7illustrates the section locations of the extractor discharge hood. In the discharge hood computational model, four planes were selected to show the wind pressure distribution at different locations. The locations of these four planes are depicted in Figure 7 (the external flow field region of the extractor is not shown). Sections A, B, and C were parallel to the ground and were positioned 500 mm, 400 mm, and 300 mm from the impeller center, respectively. Section D was located in the middle of the extractor and was parallel to the side wall of the discharge hood.

Figure 8 illustrates the dynamic pressure gradient contour plots at sections A, B, and C of the discharge hood. The central circular hole in Figure 8 represents the radial section of the drive shaft, with the airflow direction from left to right. As shown in Figure 5, a significantly low-pressure zone formed behind the drive shaft during extractor operation. The dynamic pressure contour plots indicated that the pressure distribution was not symmetrical; the dynamic pressure on the lower sidewall was higher than that on the upper sidewall. This suggested that during the operation of the extractor, sugarcane leaves and impurities were more likely to be expelled along the lower sidewall, which aligned with actual observations.

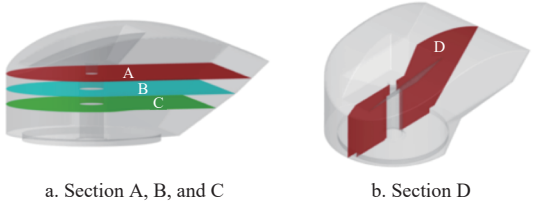

a. Section A, B, and C b. Section D

Figure 7 Section locations of extractor discharge hood

From the variations among Figures 8a-8c, it can be observed that the dynamic pressure distribution remained similar at different heights. However, the dynamic pressures at sections with heights of 300 mm and 400 mm were significantly higher than those at 500 mm. The dynamic pressure near the lower sidewall of section A ranged between 170-350 Pa, near the lower sidewall of section B between 170-470 Pa, and near the lower sidewall of section C

between 230-650 Pa. The maximum dynamic pressure was recorded at section C at a height of 300 mm, reaching 650 Pa. This indicated that the maximum wind speed during impurity removal was concentrated below one of the sidewalls.

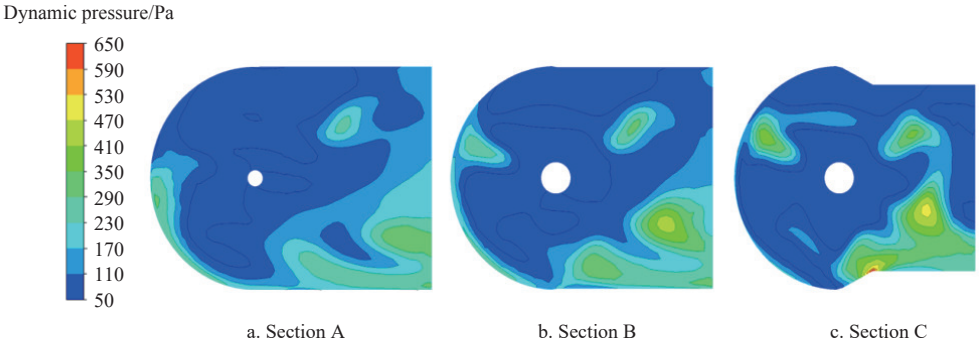

Figure 8 Dynamic pressure contour plots for sections A, B, and C

Figures 9a-9c show the static pressure, dynamic pressure, and total pressure gradient contour plots at section D of the discharge hood, respectively. According to Figure 9a, the pressure decreased along the outlet direction of the discharge hood, with lower pressure observed at the lower end of the outlet. In Figure 9b, the dynamic pressure was highest at the bottom right of section D and extended to the upper part of the outlet, while the dynamic pressure at the lower part of the outlet was significantly lower than that at the upper part. In Figure 9c the total pressure distribution mirrored the dynamic pressure distribution shown in Figure 9b. Overall, the pressure distribution at the outlet was highly uneven.

3.1.2 Analysis of wind speed in the current extractor discharge hood

From the streamline diagrams inside the discharge hood in Figures 10a-10c, it could be observed that the wind speed on the lower sidewall of sections A, B, and C was greater than that on the upper sidewall. The wind speed distribution varied slightly with the height of the sections. The lower the section height, the more uneven the wind speed distribution at the outlet. Section C exhibited the most uneven wind speed distribution, with significantly low wind speed areas in the center of the outlet and near the upper sidewall. This corroborated the dynamic pressure gradient contour plots for sections A, B, and C in Figure 8, indicating that during the operation of the impurity removal extractor, sugarcane leaves and impurities tended to be expelled along the lower sidewall. Additionally, vortex regions with very low wind speeds were present at the upper position of section B and at the left and upper positions of section C, leading to significant aerodynamic losses.

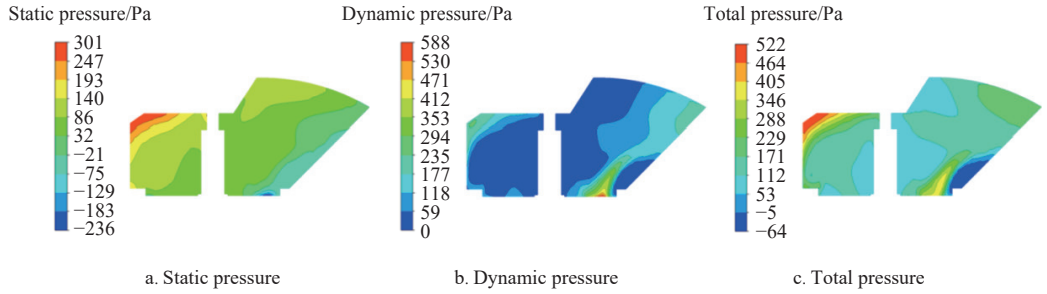

Figure 9 Static pressure, dynamic pressure, and total pressure contour plots for section D

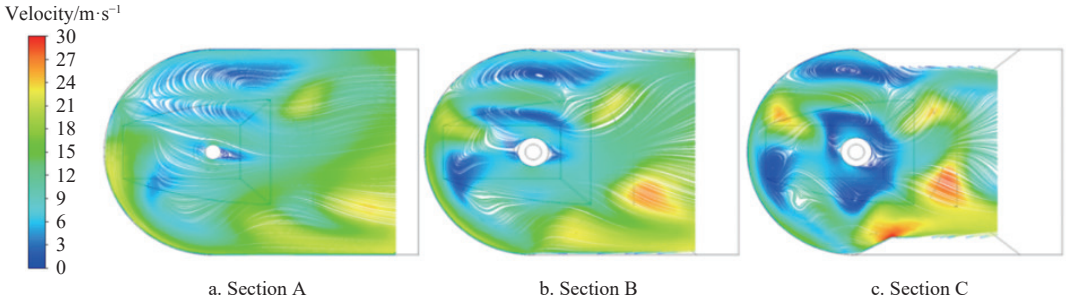

Figure 10 Wind speed streamline diagrams for sections A, B, and C

The wind speed vector diagram of the discharge hood at section D in Figure 11 indicated that the wind speed distribution was uneven. The highest wind speed, reaching 30 m/s, was observed at the bottom right of section D along the outlet direction, which aligned with the dynamic pressure gradient contour plot of section D in Figure 9b. Below the extractor outlet, the airflow separated from the inner wall of the extractor, causing a “backflow” phenomenon. This backflow obstructed the impurity removal operation of the extractor, reducing its efficiency. The likely cause of this issue was the unreasonable structural design of the extractor outlet, where the transition was not smooth enough, causing abrupt shape changes and preventing the airflow from fully adhering to the inner wall of the extractor.

Figure 12 shows the wind speed distribution contour plot at the outlet. The speed gradient variations were consistent with the dynamic pressure gradient contour plot in Figure 8, as well as the static pressure, dynamic pressure, and total pressure gradient contour plots in Figure 9. The wind speed near the left sidewall of the outlet was significantly higher than that near the right sidewall,

with the highest wind speed at the lower part of the left sidewall reaching up to 26 m/s. Conversely, the wind speed on the right half was relatively lower, with a low-speed zone appearing in the middle. This wind speed distribution also corresponded to the actual impurity removal conditions at the extractor outlet during operation.

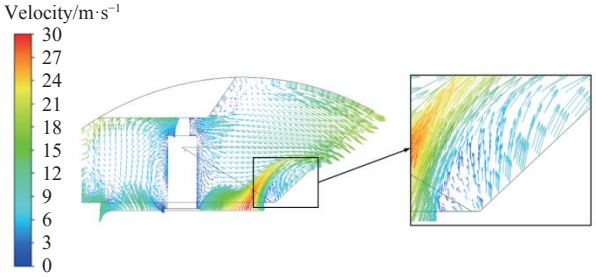

Figure 11 Wind speed vector diagram for section D

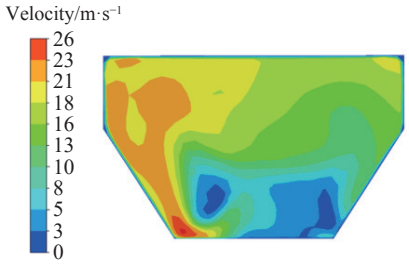

Figure 12 Wind speed gradient contour plot of the extractor outlet surface

3.2 Analysis of the internal flow field in the current extractor cleaning chamber

3.2.1 Analysis of wind pressure in the current extractor cleaning chamber

To analyze the airflow distribution within the extractor cleaning chamber, a section at $Y = 0$ mm of the cleaning chamber (Figure 13) was taken for analysis.

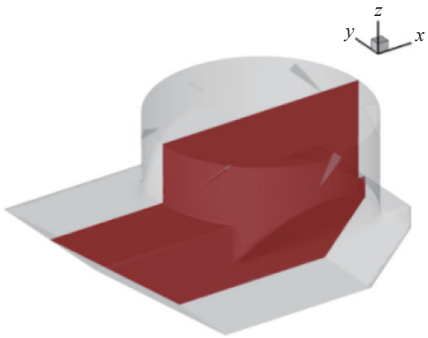

Figure 13 Section location of the extractor cleaning chamber

Figure 14 presents the gradient contour plots of static pressure, dynamic pressure, and total pressure on the $Y = 0$ cross-section of the extractor cleaning chamber. The static pressure gradient distribution contour plot in Figure 14a shows that the closer it is to the extractor blades, the greater the negative pressure, indicating that the suction generated by the rotation of the extractor blades is greater. The negative pressure near the lower end wall of the blades is significantly higher than in other areas, mainly concentrated between –511 and –284 Pa. The dynamic pressure gradient distribution contour plot in Figure 14b reveals that the closer it is to the extractor blades, the greater the dynamic pressure, with the maximum dynamic pressure reaching 632 Pa. However, there are obvious low-pressure areas below the left side of the extractor blades and near the right sidewall of the cleaning chamber. The total pressure gradient distribution contour plot in Figure 14c shows that the total pressure distribution was uniform in the central area below the cleaning chamber. However, a significant gradient change was observed near the left sidewall of the cleaning chamber, which was unfavorable for impurity removal by the extractor.

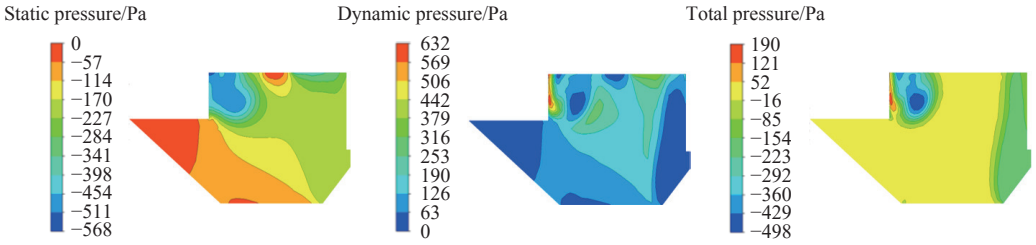

a. Static pressure b. Dynamic pressure c. Total pressure

Figure 14 Static pressure, dynamic pressure, and total pressure contour plots at $Y = 0$ mm in the cleaning chamber

3.2.2 Analysis of wind speed in current extractor cleaning chamber

Figure 15 illustrates the wind speed streamline diagram on the $Y = 0$ cross-section in the extractor cleaning chamber. A large vortex area was generated near the left outlet of the cleaning chamber. This vortex generally represented a flow dead zone, meaning it did not participate in the main flow movement but only rotated in place. Additionally, a low-speed area was observed near the lower right side of the extractor cleaning chamber, which also exhibited obvious vortex characteristics. This further increased aerodynamic losses for the impurity removal extractor. The formation of vortices was attributed to a significant angle change at the transition between the left inlet and the cleaning chamber wall, causing airflow collisions between the lower inlet and the left inlet of the extractor, leading to vortex formation. Furthermore, a low-speed vortex area was present near the lower right side of the cleaning chamber, which was similarly caused by a significant angle change in shape.

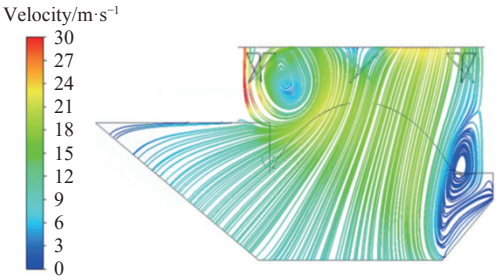

Figure 15 Wind speed streamline diagram at $Y = 0$ mm in cleaning chamber

4 Structure optimization and simulation results analysis of the extractor

4.1 Structure optimization of the extractor

Based on the analysis results of the current extractor's flow field, the discharge hood and cleaning chamber shapes in the extractor structure were optimized. To eliminate the abrupt shape changes in the discharge hood, the external contour of the optimized discharge hood was designed as a smooth arc curve, allowing the airflow to adhere more closely to the inner wall during movement, thereby reducing significant airflow disturbances. The simplified structural diagram of the optimized impurity removal extractor is presented in Figure 16, and the corresponding parameters are listed in Table 3.

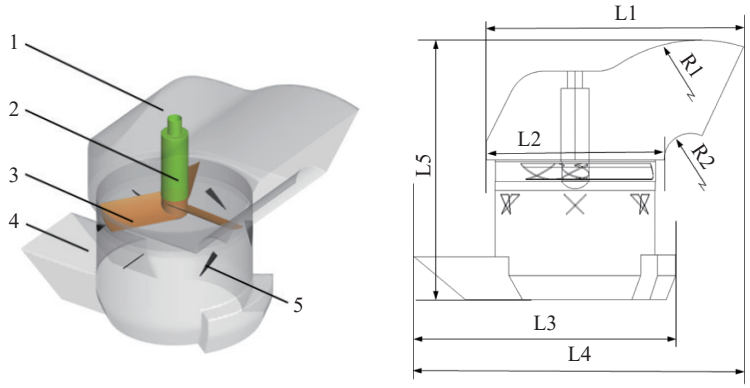

a. Simplified structural diagram of the optimized extractor

b. Structural parameters of the optimized extractor

1. Discharge hood 2. Drive shaft 3. Extractor blades 4. Cleaning chamber 5. Deflector plate

Figure 16 Structure diagram of optimized extractor

Table 3 Main parameters of optimized extractor

Parameters	Values	Parameters	Values
Diameter of impeller/mm	850	Length of L2/mm	1000
Number of blades	3	Bending radius of upper outlet of discharge hood R1/mm	800
Diameter of extractor/mm	900	Bending radius of lower outlet of discharge hood R2/mm	150
Number of deflectors	6	Length of L3/mm	1570
Rotation speed /(r/min)	1250-1650	Length of L4/mm	2060
Length of L1/mm	1550	Height of extractor L5/mm	1500

4.2 Analysis of the simulation results of the optimized extractor

The optimized extractor model was analyzed at four sections: those located at 500 mm, 400 mm, and 300 mm (Z=500 mm, 400 mm, 300 mm) from the impeller center, and the Y = 0 mm section. It was found that the dynamic pressure within the optimized extractor discharge hood (Figure 17) had significantly improved in both value and uniformity compared to the current extractor. Additionally, the wind speed streamline diagram inside the discharge hood (Figure 18) demonstrated that the optimized extractor exhibited higher wind speeds and better uniformity than the current extractor, with vortex areas greatly reduced and only a small vortex remaining at the Z = 300 mm section.

In the current extractor, the transition below the outlet was not smooth enough, resulting in an abrupt shape change. This prevented the airflow from fully adhering to the inner wall of the extractor, leading to a "backflow" phenomenon at the discharge hood outlet that negatively impacted impurity removal. After optimization, the

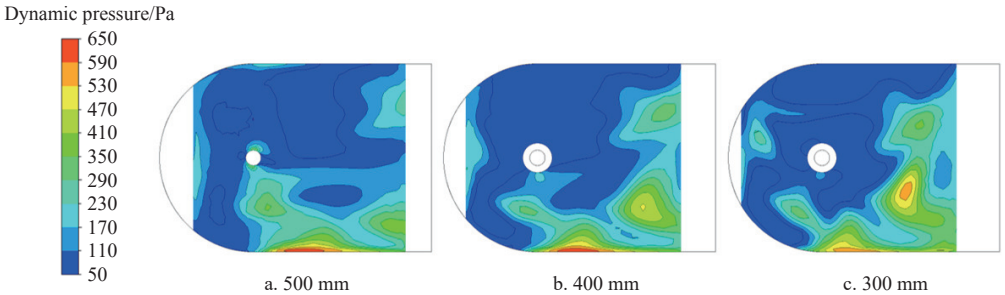

a. 500 mm b. 400 mm c. 300 mm

Figure 17 Dynamic pressure contour plots of the optimized discharge hood at sections Z=500 mm, 400 mm, and 300 mm

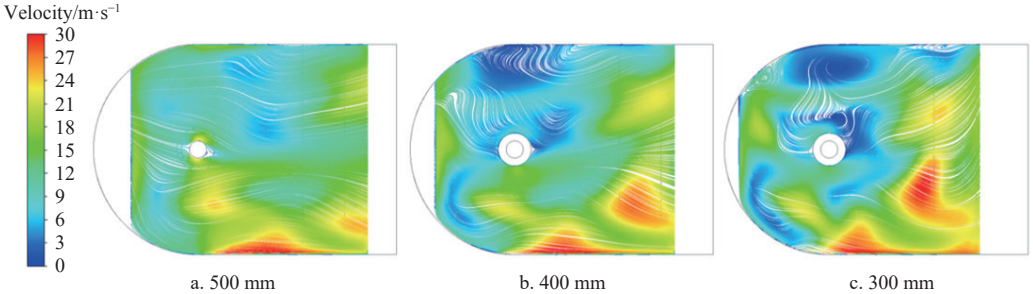

a. 500 mm b. 400 mm c. 300 mm

Figure 18 Wind speed streamline diagrams of the optimized discharge hood at sections Z=500 mm, 400 mm, and 300 mm

transition below the discharge hood outlet was modified to a curved wall. As shown in the airflow vector diagram (Figure 19), the optimized airflow adhered more closely to the outlet wall, increased in speed, and eliminated the "backflow" phenomenon at the outlet.

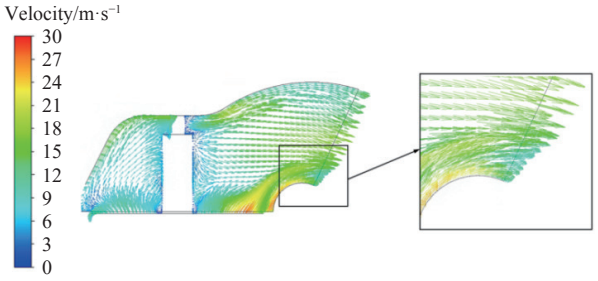

Figure 19 Wind speed vector diagram of the optimized discharge hood at the $Y = 0$ section

Figure 20 shows the wind speed distribution contour plot at the outlet of the optimized extractor. Compared with the current extractor, the optimized outlet section exhibited a higher and more uniform wind speed. In addition, the introduction of a curved transition at the discharge hood outlet eliminated the significant low-speed region that had been present below the outlet in the current extractor, making it more favorable for impurity removal.

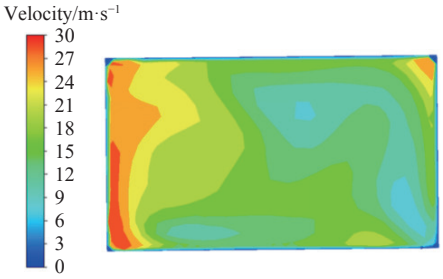

Figure 20 Wind speed gradient contour plot of the optimized extractor outlet

Figure 21 shows the wind speed streamline diagram at the $Y = 0$ section of the optimized extractor cleaning chamber. Compared with the current extractor, the wind speed in the optimized cleaning chamber decreased locally; however, the overall wind speed increased significantly, and the distribution within the cleaning chamber became more uniform, which was beneficial for impurity removal. The optimized cleaning chamber eliminated the large vortex area near the left outlet that had been observed in the current extractor, thereby preventing the collision and accumulation of sugarcane leaves within the cleaning chamber during impurity removal. Although a small low-speed vortex area still existed in the lower right of the optimized cleaning chamber, it was smaller in size and further removed from the main impurity removal area (left inlet and center cylinder) than in the current extractor, and thus it was not expected to have a significant impact on impurity removal during sugarcane harvesting.

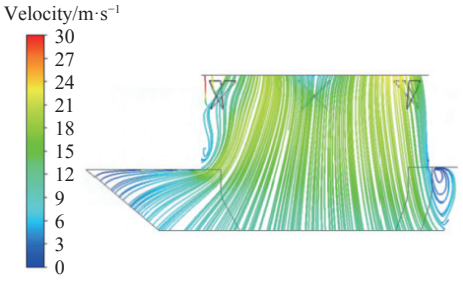

Figure 21 Wind speed streamline diagram at $Y = 0$ mm in the optimized cleaning chamber

4.3 Comparison of aerodynamic performance between current extractor and optimized extractor

To analyze the aerodynamic performance differences of the current extractor and optimized extractor, the total pressure and total pressure efficiency were calculated. The calculation formula is as follows:

$$P_t = P_{out} - P_{in} \tag{6}$$

$$P_1 = \frac{n \times T}{9550} \tag{7}$$

$$P_2 = \frac{P_t \times Q}{1000} \tag{8}$$

$$\eta = \frac{P_2}{P_1} = \frac{P_t \times Q \times 9550}{1000 \times n \times T} \tag{9}$$

where, P_t is the total pressure of the extractor, Pa; P_{out} is the total pressure at the extractor outlet, Pa; P_{in} is the total pressure at the extractor inlet, Pa; η is the total pressure efficiency of the extractor, %; Q is the extractor flow rate, m³/s; P_1 is the shaft power of the extractor, kW; P_2 is the effective power of the extractor, kW; T is the impeller torque, N·m; n is the extractor speed, r/min.

Based on practical engineering considerations, the no-load flow rates at extractor speeds of 1250, 1450, and 1650 r/min, as well as the total pressure and total pressure efficiency at different flow rates, were calculated. As shown in Figure 22a, the no-load flow rates of the optimized extractor increased by 15.85%, 17.06%, and 16.43% at 1250, 1450, and 1650 r/min, respectively, compared with the current extractor. Figure 22b demonstrates that the optimized

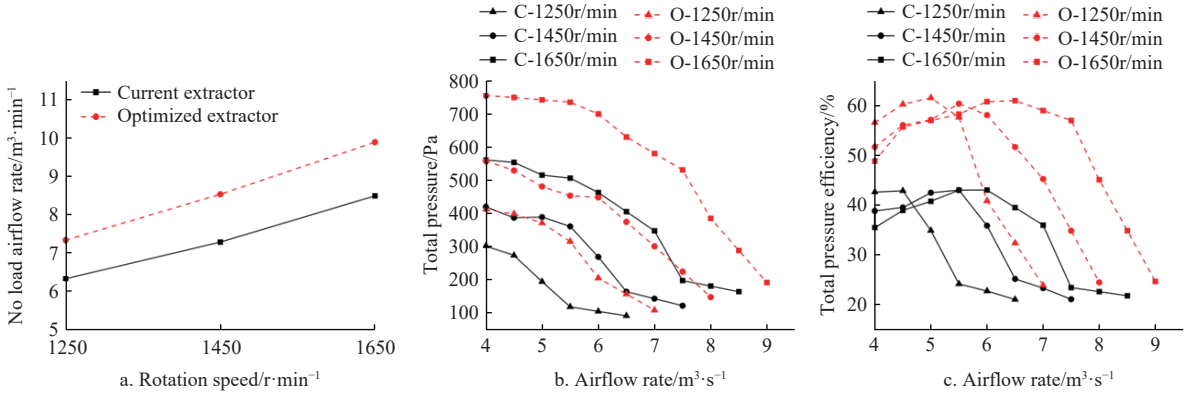

Figure 22 Performance curves of the current extractor and the optimized extractor

extractor exhibited a higher total pressure at all flow rates, indicating a stronger capacity for conveying impurities and suggesting that it could handle higher feed rates. Furthermore, Figure 22c reveals that the maximum efficiency of the current extractor at speeds of 1250, 1450, and 1650 r/min was only 42.87%, 43.02%, and 43.04%, respectively, while the maximum efficiency of the optimized extractor increased by 15.24%, 15.31%, and 15.63% at these speeds, respectively, indicating a higher energy utilization rate.

5 Field test of extractor performance

The optimized extractor improved the pressure and flow velocity inside the unit, while also enhancing the uniformity of the wind speed distribution at the outlet, thereby increasing the effective utilization area of the outlet surface. Simulation results (Figure 22) indicated that, at the same speed, the optimized extractor provided higher flow and total pressure, which was beneficial for impurity separation and consequently reduced the impurity rate. To verify the effect of the extractor optimization, a test was conducted in Fusui County, Guangxi Zhuang Autonomous Region, in December 2023. The sugarcane variety used for the field test was Gui Sugar 44, and the test harvester was the 4GQ-180 segment-type sugarcane harvester from Luoyang Chenhan Agricultural Equipment Technology Co., Ltd. The test site is shown in Figure 23.

Figure 23 Test site and environment

5.1 Method for determining impurity rate and cane loss rate

The evaluation indicators for the field test were impurity rate and cane loss rate. Preliminary experiments found that when the harvester's travel speed reached 4 km/h, the conveying mechanism was prone to blockage; therefore, the impurity rate and cane loss rate were measured at travel speeds below 4 km/h. The experimental factors and levels are presented in Table 4. During operation, a colored canopy cloth bag (with one end tied and the other end placed over the extractor outlet) was used to collect impurities discharged by the impurity-removal extractor; the harvested sugarcane material fell into the collection box, and materials were collected using a colored canopy cloth, as shown in Figure 24. The specific test steps were conducted in accordance with JB/T 6275-2019 test methods for sugarcane harvesting machinery[30].

The impurity rate and cane loss rate can be calculated as:

$$P_i = \frac{m_i}{m_i + m_t} \times 100\% \tag{10}$$

$$P_l = \frac{m_b}{m_b + m_t} \times 100\% \tag{11}$$

where, P_i is the impurity rate, %; m_i is the mass of impurities in the collection box, kg; m_t is the total mass of sugarcane in the collection box, kg; P_l is the cane loss rate, %; m_b is the mass of sugarcane in the cloth bag at the outlet, kg.

Table 4 Field experimental factors and levels

Experimental factors	Levels		
Extractor speed/r·min^{-1}	1250	1450	1650
Travel speed/km·h^{-1}	1	2	3

Figure 24 Determination of impurity rate, cane loss rate

5.2 Experimental results and analysis

Table 5 presents the results of impurity rate and cane loss rate in the field experiment. The field test results of impurity rate are shown in Figure 25. When the extractor speed was 1250 r/min and the travel speed was 1 km/h (Figure 25a), the impurity rate of sugarcane using the optimized extractor was reduced compared to that of the current extractor, but the reduction was small—only 9.73%. This was because the low travel speed of the harvester led to a low feed rate, resulting in a low extractor load. Under low load conditions, the current extractor was also capable of maintaining a high de-impurity performance. However, when the harvester's travel speed increased to 2 km/h, more sugarcane segments and leaf impurities entered the extractor, thereby increasing the extractor load. At the same speed, the optimized extractor provided higher flow and pressure, and its impurity rate was significantly reduced compared to that of the current extractor, with a reduction of 21.52%. When the travel speed reached 3 km/h, the difference in impurity rate between the optimized extractor and the current extractor further increased, with the impurity rate of the optimized extractor reduced by 28.30%.

Table 5 Results of impurity rate and cane loss rate in field experiment

Extractor speed/r·min^{-1}		Travel speed/km·h^{-1}	m_i/kg	m_b/kg	m_t/kg	P_i/%	P_l/%
1250	Current	1	3.94	4.61	61.35	6.03	6.98
		2	4.54	4.01	55.20	7.61	6.77
		3	5.70	3.74	57.51	9.01	6.11
	Optimized	1	3.89	4.84	67.54	5.44	6.69
		2	3.86	4.16	60.75	5.97	6.41
		3	3.91	3.44	56.65	6.46	5.73
1450	Current	1	3.39	5.06	58.46	5.48	7.97
		2	3.95	4.30	58.88	6.29	6.81
		3	4.70	3.91	58.00	7.50	6.32
	Optimized	1	3.48	4.93	64.32	5.13	7.11
		2	3.07	3.55	52.08	5.56	6.38
		3	3.11	3.14	48.69	6.01	6.05
1650	Current	1	3.10	5.87	59.16	4.98	9.03
		2	2.84	4.52	50.98	5.27	8.14
		3	3.58	4.44	53.34	6.29	7.68
	Optimized	1	2.82	5.06	56.37	4.76	8.24
		2	2.76	4.20	51.99	5.03	7.47
		3	2.84	3.61	47.19	5.67	7.11

At an extractor speed of 1450 r/min (Figure 25b), the difference in impurity rate between the current extractor and the optimized extractor was not significant. However, when the harvester's travel speed increased to 3 km/h, the increased workload of the extractor

led to a larger difference in impurity rate before and after optimization, with the impurity rate of the optimized extractor reduced by 19.84% compared to the current extractor.

At an extractor speed of 1650 r/min, the gap in impurity rate between the optimized extractor and the current extractor at travel speeds of 1 km/h, 2 km/h, and 3 km/h was relatively small, with the maximum reduction in impurity rate being only 9.86%. This occurred because, as the extractor speed increased, both extractors generated higher wind speeds and pressures, which effectively expelled impurities. Analysis of Figure 25 shows that the de-impurity performance of the optimized extractor at high speed (1650 r/min) was comparable to that of the current extractor. However, when both extractors operated at medium (1450 r/min) and low (1250 r/min) speeds, the impurity rate of the optimized extractor was significantly lower than that of the current extractor, demonstrating its superior de-impurity performance.

Figure 26 presents the results of the field test regarding cane loss rate. At an extractor speed of 1250 r/min (Figure 26a), the cane loss rates for both extractors at travel speeds of 1 km/h, 2 km/h, and 3 km/h were very similar, with the optimized extractor exhibiting a reduction of up to 6.27% compared to the current extractor. This result was attributed to the relatively low flow and pressure generated by both extractors at this speed, which had only a minor impact on sugarcane loss.

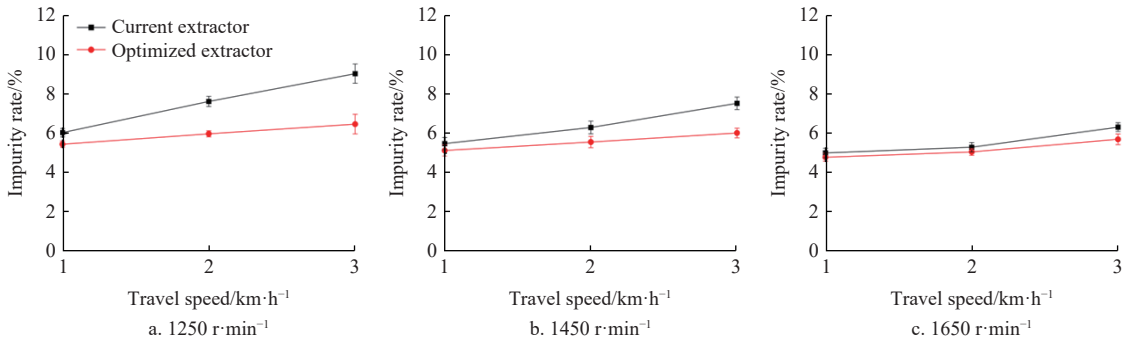

Figure 25 Impurity rate of the current extractor and the optimized extractor

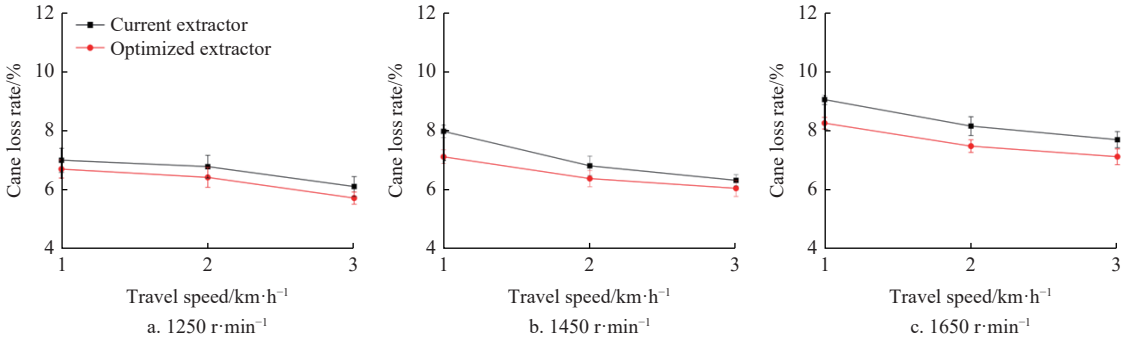

Figure 26 Cane loss rate of the current extractor and the optimized extractor

When the extractor speed was increased to 1450 r/min (Figure 26b), the cane loss rate of the optimized extractor was significantly reduced across all travel speeds. Moreover, at a travel speed of 1 km/h, the reduction was more pronounced, reaching a maximum decrease of 10.75%. This improvement was due to the low load condition, where the high wind speed and the presence of numerous sugarcane fragments increased the likelihood of sugarcane ejection in the current extractor; in contrast, the arc plate at the outlet of the optimized extractor partially blocked the expulsion of these fragments.

At an extractor speed of 1650 r/min (Figure 26c), the optimized extractor demonstrated a cane loss rate that was up to 8.78% lower than that of the current extractor at travel speeds of 1 km/h, 2 km/h, and 3 km/h. However, the difference between the two extractors was less pronounced compared to the medium speed (1450 r/min) because, at the higher extractor speed, both extractors generated very high wind speeds and pressures, which tended to draw sugarcane into the impeller area. The resulting collisions broke the sugarcane and expelled fragments, thereby increasing the overall cane loss rate.

6 Conclusions

To reduce the impurity rate and cane loss rate in the mechanized harvesting of sugarcane, the extractor of sugarcane harvester was taken as the research object. Through CFD simulation, the structural defects of the extractor were analyzed and the structure was improved. The conclusions were as follows:

(1) The simulation model demonstrated high accuracy, with a maximum error of 5.29% and an average error of 4.71% in the outlet average wind speed. This validates the reliability of the simulation approach for further design improvements.

(2) The structure of the extractor was optimized, with changes including a smooth transition surface at the top of the guide hood and the addition of a circular arc transition plate beneath the outlet. These adjustments eliminated large airflow vortices and the backflow phenomenon within the extractor, resulting in improved wind speed and better airflow uniformity. Additionally, the structure of the cleaning chamber was optimized to reduce vortices and improve the uniformity of airflow inside the chamber. These modifications led to higher flow rates, better total pressure, and more efficient energy utilization.

(3) The impurity rate test demonstrated that at a harvester speed of 1 km/h, the impurity rates before and after optimization were comparable at different rotational speeds. At 2 km/h, the performance of the optimized extractor at low rotation speed (1250 r/min) showed a 21.52% improvement. At 3 km/h, the

optimized extractor at both medium (1450 r/min) and low rotational speeds showed a significant reduction in impurity rates, with reductions of 19.84% and 28.30%, respectively. These improvements highlighted the potential of the optimized extractor to significantly reduce impurity rate, even under varying operational conditions.

(4) The cane loss rate test revealed that at 1250 r/min, there was little difference between the cane loss rates before and after optimization across different driving speeds. However, at 1450 r/min, the optimized extractor significantly reduced the cane loss rate, with the maximum reduction observed at 10.75%. At 1650 r/min, the optimized extractor also showed reduced cane loss rates across all driving speeds, though the reduction was less significant compared to the medium-speed condition (1450 r/min), with the maximum reduction being 8.78%.

The optimized extractor significantly reduced the impurity rate and cane loss rate at higher harvester speeds (2-3 km/h), which makes it suitable for large-scale and high-speed harvesting operations that are crucial for the mechanized sugarcane harvesting industry. Moreover, the optimized design is expected to contribute to substantial operational benefits. By reducing waste through lower cane loss and impurity rates, the design offers the potential to lower processing costs and increase the efficiency of mechanized sugarcane harvesting. These improvements are especially valuable for large-scale operations where consistent performance and energy efficiency are critical. Overall, the results of this study provide a clear pathway for the further design and optimization of sugarcane harvesters, which will help to improve harvesting quality, reduce operational costs, and contribute to the advancement of agricultural mechanization.

Acknowledgements

The research presented in this paper was partially supported by the Guangxi Sugarcane Science and Technology Project (Guike AA22117005-1), the Hainan Natural Science Foundation Innovative Research Team Project (Grant No. 322CXTD521), the Guangxi Innovation-Driven Development Project (Guike AC22080001), the National Natural Science Foundation of China (Grant No. 32071916), and the Guangxi Sugarcane Science and Technology Project (Grant No. 2022AA01010).

[References]

[1] Zhao H, Sun D, Lu Y. Recent situation, hot spot analysis and prospect of sugarcane research in China. Sugarcane Sugar Ind., 2018; 20: 65–70. (in Chinese)

[2] Zhou Y, Yang L, Bo M. Analysis of yield difference and its influencing factors in main sugarcane producing areas of China. China Agric. Sci., 2021; 54: 2377–2388. (in Chinese)

[3] Wei Q, Yang B, Gao Z. Analysis on the present situation of sugarcane industrialization in China. Agric. Mech. Res., 2015; 37: 247–254. (in Chinese)

[4] Zhang C, Lu H. Current situation and suggestions of mechanized sugarcane harvesting in Guangxi. Agric. Eng., 2019; 9: 5–9. (in Chinese)

[5] Kishore N, Gayathri D, Venkatesh J. Present mechanization status in sugarcane: A review. Int. J. Agric. Sci., 2017; 9: 4247–4253. https://api.semanticscholar.org/CorpusID:268427724

[6] Fan Q, Huang Q, Wu H. Overview and prospect of sugarcane harvesting mechanization at home and abroad. Sugarcane Sugar Ind., 2020; 49: 1–11. (in Chinese)

[7] Liu Q T, Huang Y, Jiang J L. Review of sugarcane mechanized harvesting technology and equipment. Transactions of the CSAM, 2024; 55(12): 1–21. (in Chinese)

[8] Huo P, Ma S C, Su C Y, Ding Z L, Li W Q, Qian J, et al. Sugarcane leaf-stalk separating technology: A critical review. Biosystems Engineering, 2023; 228: 120–148.

[9] Whiteing C, Norris C P, Paton D C. Extraneous matter versus cane loss: Finding a balance in chopper harvested green cane. Sugar Cane Tech, 2001; 24(2): 276–282.

[10] Sichter N J, Whiteing C, Bonaventura P. Estimation of harvester losses by determination of sugar in harvest residue. International Sugar Journal, 2006; 108(1288): 218–222

[11] Viator R P, Richard E P, Viator B J. Sugarcane chopper harvester extractor and ground speed effects on yield and quality. Appl. Eng. Agric., 2007; 23(1): 31–34.

[12] Wang F, Yang G, Ke W. Studies on suspension property of sugarcane components. IFAC-Papers On Line, 2018; 51(17): 526–531.

[13] Huang Z, Sun F Y, Huang S X, Yang D T. Fluent simulation of inner-flow-field of axial-excluder devices for sugarcane harvester. J Agric Mechaniz Res, 2017; 39(3): 32–36. (in Chinese)

[14] Nong H, Zeng B, Mo J. Simulation of internal flow field of sugarcane harvester impurity removal device based on SolidWorks flow simulation. Agric Eng, 2017; 4: 133–137. (in Chinese)

[15] Zhou B C, Ma S C, Li W Q, Li W Z, Peng C. Study on the influence mechanism of energy consumption of sugarcane harvester extractor by fluid simulation and experiment. Agriculture, 2023; 13(9): 1726.

[16] Xie F X, Ou Y G, Liu Q T, Zou X P, Feng J M. Design and test of exhaust extractor for sugarcane harvester. Transactions of the CSAE, 2012; 28(25): 8–14. (in Chinese)

[17] Wang H, Li S, Ma E. Pneumatic design of impurity removal extractor for small sugarcane harvester. Agric Mechaniz Res, 2015; 37(10): 103–107. (in Chinese)

[18] Xing H N, Ma S C, Mo J L, Zeng B S, Liang W P, Li W Q, et al. Optimization and experiment of parameters for the impeller structure of extractor in a sugarcane chopper harvester. Transactions of the CSAE, 2021; 37(12): 12–19. (in Chinese)

[19] Xing H N, Ma S C, Wang F L, Bai J, Ma J. Aerodynamic performance evaluation of sugarcane harvester extractor based on CFD. Sugar Tech, 2021; 23: 627–633.

[20] Xing H N, Ma S C, Wang F L, Bai J, Hu J. Improving the performance of a sugarcane harvester extractor using design changes validated by computational fluid dynamic modelling and experiment. Biosystems Engineering, 2022; 218: 124–138.

[21] Ren J, Wu T, Liu Q, Zou X, Li K. Design and test of the structure of extractor negative pressure zone of sugarcane chopper harvester. Agronomy, 2022; 12(10): 2336.

[22] Wang C, Ning X, Wang C. Cross-flow extractor with double-channel herringbone inclined impeller of combine harvester. Transactions of the CSAM, 2013; 44(2): 17–21. (in Chinese)

[23] Gebrehiwot M G, Baer J D, Baelmans M. Effect of a cross-flow opening on the performance of a centrifugal extractor in a combine harvester: Computational and experimental study. Biosystems Engineering, 2010; 105(2): 247–256.

[24] Tong S, Shen Q, Tang N, Jia Y, Cong F, Gu W. Numerical simulation and optimization test of mixed flow field in longitudinal axial flow cleaning device. Transactions of the CSAM, 2016; 47(7): 135–142. (in Chinese)

[25] Zhang S. Principles and Applications of CFD Technology. Wuhan: Huazhong University of Science and Technology Press, 2016. (in Chinese)

[26] Xu H Y, Guo J H. Direct numerical simulation analysis of turbulence in square and rectangular annular tubes: II. Reynolds stress field and mean energy spectrum, a re-conceptualization of the traditional turbulence ontology relationship. Sci China Phys Mech Astron, 2017; 47(8): 113–129. (in Chinese)

[27] Wu S, Zhang J. Determination of inlet conditions in direct simulation of turbulent premixed jet flames. J Tsinghua Univ (Nat Sci Ed), 2014; 54(6): 834–838. (in Chinese)

[28] Su Y, Splitter D, Kim S H. Laminar-to-turbulent flame transition and cycle-to-cycle variations in large eddy simulation of spark-ignition engines. Int J Engine Res, 2021; 22(9): 2803–2818.

[29] Farges B, Gauffre M C, Benhamadouche S, Badel P, Faucher V, Ricciardi G. Advanced benchmark of the flow through a mixing vane grid—Large eddy simulation validation. Nucl Eng Des, 2021; 381: 1113335.

[30] National Development and Reform Commission of the People's Republic of China. JB/T 6275-2019. Test methods for sugarcane harvesting machinery. Beijing: China Standard Press, 2019. (in Chinese)